

# Evaluation of S-values and dose distributions for $^{90}\text{Y}$ , $^{131}\text{I}$ , $^{166}\text{Ho}$ , and $^{188}\text{Re}$ in seven lobes of the rat liver

Tianwu Xie

*Britton Chance Center for Biomedical Photonics, Wuhan National Laboratory for Optoelectronics, Huazhong University of Science and Technology, Wuhan 430074, People's Republic of China and Key Laboratory of Biomedical Photonics of Ministry of Education, Huazhong University of Science and Technology, Wuhan 430074, China*

Qian Liu<sup>a)</sup>

*Britton Chance Center for Biomedical Photonics, Wuhan National Laboratory for Optoelectronics, Huazhong University of Science and Technology, Wuhan 430074, People's Republic of China; Key Laboratory of Biomedical Photonics of Ministry of Education, Huazhong University of Science and Technology, Wuhan 430074, China; and Division of Nuclear Medicine and Molecular Imaging, Geneva University Hospital, CH-1211 Geneva, Switzerland*

Habib Zaidi

*Division of Nuclear Medicine and Molecular Imaging, Geneva University Hospital, CH-1211 Geneva, Switzerland; Geneva Neuroscience Center, Geneva University, CH-1211 Geneva, Switzerland; and Department of Nuclear Medicine and Molecular Imaging, University Medical Center Groningen, University of Groningen, 9700 RB Groningen, The Netherlands*

(Received 5 September 2011; revised 11 January 2012; accepted for publication 11 January 2012; published 27 February 2012)

**Purpose:** Rats have been widely used in radionuclide therapy research for the treatment of hepatocellular carcinoma (HCC). This has created the need to assess rat liver absorbed radiation dose. In most dose estimation studies, the rat liver is considered as a homogeneous integrated target organ with a tissue composition assumed to be similar to that of human liver tissue. However, the rat liver is composed of several lobes having different anatomical and chemical characteristics. To assess the overall impact on rat liver dose calculation, the authors use a new voxel-based rat model with identified suborgan regions of the liver.

**Methods:** The liver in the original cryosectional color images was manually segmented into seven individual lobes and subsequently integrated into a voxel-based computational rat model. Photon and electron particle transport was simulated using the MCNPX Monte Carlo code to calculate absorbed fractions and S-values for  $^{90}\text{Y}$ ,  $^{131}\text{I}$ ,  $^{166}\text{Ho}$ , and  $^{188}\text{Re}$  for the seven liver lobes. The effect of chemical composition on organ-specific absorbed dose was investigated by changing the chemical composition of the voxel filling liver material. Radionuclide-specific absorbed doses at the voxel level were further assessed for a small spherical hepatic tumor.

**Results:** The self-absorbed dose for different liver lobes varied depending on their respective masses. A maximum difference of 3.5% was observed for the liver self-absorbed fraction between rat and human tissues for photon energies below 100 keV.  $^{166}\text{Ho}$  and  $^{188}\text{Re}$  produce a uniformly distributed high dose in the tumor and relatively low absorbed dose for surrounding tissues.

**Conclusions:** The authors evaluated rat liver radiation doses from various radionuclides used in HCC treatments using a realistic computational rat model. This work contributes to a better understanding of all aspects influencing radiation transport in organ-specific radiation dose evaluation for preclinical therapy studies, from tissue composition to organ morphology and activity distribution.  
© 2012 American Association of Physicists in Medicine. [DOI: 10.1118/1.3681009]

Key words: radionuclide therapy, rat liver, computational models, Monte Carlo, dose-volume histogram, S-values

## I. INTRODUCTION

The liver is the largest solid organ in both human and rat bodies, having a complex anatomical structure and performing various vital functions (e.g., protein metabolism, plasma protein synthesis, and chemical neutralization).<sup>1,2</sup> The liver is considered as an important dose-limiting tissue, especially in radiotherapy for hepatocellular carcinoma (HCC),<sup>3</sup> which is the most common solid organ tumor worldwide.<sup>4,5</sup> At

present, various radiopharmaceuticals have been developed for radionuclide therapy of HCC.<sup>6</sup>  $^{131}\text{I}$  is utilized in most clinical research studies and has been reported to produce much better treatment tolerance than traditional chemoembolization, with few undesirable effects (such as fever, reversible leukopenia, etc.) observed.<sup>6,7</sup>  $^{90}\text{Y}$  is a widely used typical long-range  $\beta$ -emitting radionuclide for various cancer therapies,<sup>8</sup> and its use for the treatment of HCC with  $^{90}\text{Y}$ -labeled microspheres (such as glass microsphere, resin

microsphere, plastic microsphere, etc.) reported in the literature.<sup>9–12</sup> <sup>188</sup>Re is an emerging and safe effective radionuclide for therapy of HCC<sup>13</sup>; however, detailed dosimetry data for animals and patients are still required.<sup>14,15</sup> Mumper *et al.*<sup>16</sup> suggested <sup>166</sup>Ho as a potential agent for radiation therapy of liver cancer. Nijssen *et al.*<sup>17</sup> implanted 0.5–1 mm<sup>3</sup> tumor-tissue in the liver of 15 rats and injected 20–50 μm <sup>166</sup>Ho-labeled microspheres into the hepatic artery for biodistribution studies.

Rats are widely used in preclinical trials of new radiopharmaceuticals for HCC treatment where the relationship between the absorbed dose and biological response is sought.<sup>18–21</sup> Two methods are usually employed to evaluate organ absorbed dose to animal models. The first uses implanted dosimeters,<sup>22,23</sup> whereas the second relies on computer simulations using anatomical computational animal models.<sup>24,25</sup> The sensitivity and accuracy of radiation dosimeters are known to be affected by environmental factors (e.g., relative humidity and temperature) and irradiation conditions.<sup>26–28</sup> With advances in computer technology and availability of Monte Carlo simulation packages, human and animal computational anatomical models have gained popularity for the assessment of absorbed dose.<sup>29</sup> For this purpose, the anatomical information (e.g., volume, mass, and shape) is combined with tissue densities and chemical compositions of the computational model to simulate radiation interaction with biological tissues.

Kolbert *et al.*<sup>30</sup> evaluated mouse-specific S-values for the liver, spleen, and kidney of five radionuclides. Funk *et al.*<sup>31</sup> investigated the radiation dose delivered to small animals from various radionuclides used in SPECT and PET imaging using mouse and rat sized ellipsoids assumed to consist of soft tissue analog.<sup>32</sup> Bitar *et al.*<sup>33</sup> calculated the absorbed dose to organs of a mouse model using the MCNP code. Peixoto *et al.*<sup>34</sup> and Xie *et al.*<sup>35,36</sup> developed novel voxel-based rat models for radiation transport calculations and calculated the internal absorbed dose to various organs of their models. Recently, Stabin *et al.*<sup>37</sup> and Keenan *et al.*<sup>38</sup> reported a series of realistic small animal models designed specifically for preclinical dose assessment studies.

The accurate calculation of absorbed dose to organs of interest depends on the computational model that should mimic the anatomical, physical, and chemical features of humans and small animal.<sup>24,25</sup> In previous radiation dose calculations, the rat liver is commonly considered as a homogeneous integrated target organ, and its tissue composition is usually assumed to be equivalent to human tissues. However, the rat liver is composed of several anatomical compartments, and some discrepancies in terms of anatomical and chemical characteristics, such as mass, shape, and chemical composition between these liver lobes, have been reported.<sup>39,40</sup> Garcia-Moreno *et al.*<sup>41</sup> suggested that there might be a functional heterogeneity between the various hepatic lobes. Little attention has been paid to the absorbed dose of different rat liver lobes and the influence of chemical composition on radiation dose estimations. Moreover, some biodistribution studies of radiolabeled microspheres for HCC therapy of the rat reported that the microspheres are

mainly restricted to the liver lobe where the tumor is implanted.<sup>17</sup> This suggests that the whole liver may not be the best target region for radiation dose calculation in radiation therapy experiments for rat liver tumors.

In this paper, a voxel-based rat model consisting of 22 identified tissue regions is presented. The liver of this model was divided into seven portions for internal radiation dose estimations. Radiation transport for photons and electrons was simulated in the rat model, and the absorbed doses to the seven identified liver lobes of the rat liver were calculated. The objectives of this study are threefold: (1) to study photon and electron absorbed fractions in different regions of the rat liver using Monte Carlo calculations, (2) to investigate the effects of chemical composition on rat organ radiation dose calculation, and (3) to provide detailed absorbed dose data for radionuclide therapy of HCC for rat studies.

## II. MATERIALS AND METHODS

### II.A. The voxel-based rat model and identified liver lobes

A 153 g Sprague-Dawley rat was used in our study.<sup>42</sup> A total of 1646 axial successive color photographic images were collected using a high-quality cryosectional imaging system.<sup>43</sup> The original voxel dimensions were 0.02 × 0.02 × 0.1 mm<sup>3</sup> and were increased to 0.1 × 0.1 × 0.1 mm<sup>3</sup> for radiation dose calculations to circumvent computational memory limitations. Manual segmentation was performed using Adobe Photoshop<sup>TM</sup> (Adobe Systems, San Jose, CA). The left kidney, right kidney, liver, lungs, spleen, heart, stomach, brain, spinal cord, thyroid, thymus, skeleton, eyes, esophagus, pancreas, and blood were identified and delineated. Figure 1 shows 3D views of the voxel-based rat model with semitransparent skin and skeleton. The liver region of this model was further divided into seven anatomically distinct regions (lobus sinister

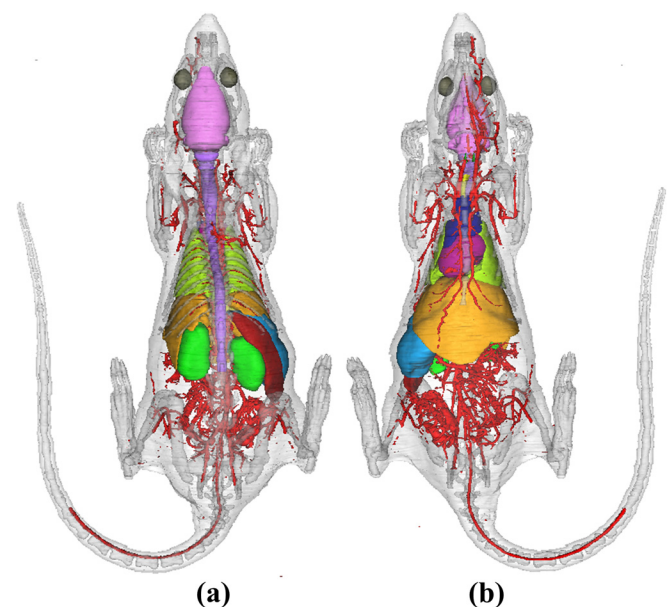


FIG. 1. (a) Dorsal and (b) ventral views of the voxel-based rat phantom with semitransparent skin and skeleton.

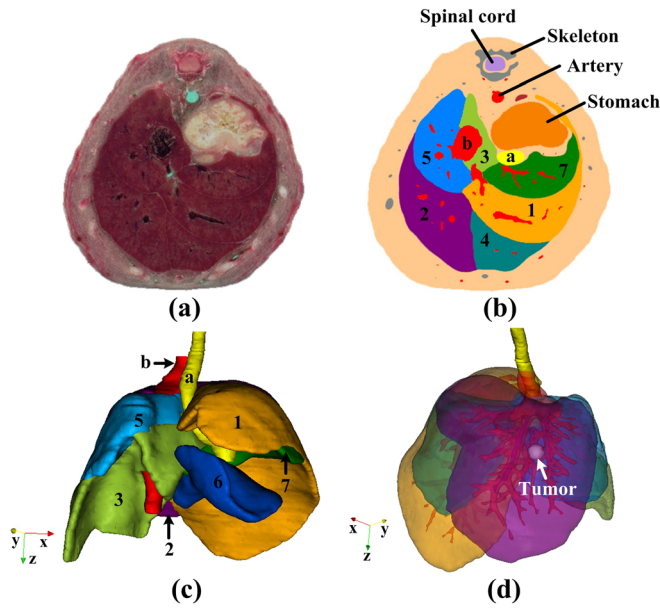


Fig. 2. The original and segmented images of the rat phantom and the 3D anterior and 540 posterior views of the liver region. (a) The original color image of one slice at abdomen level and (b) the segmented atlas image of the same slice. (c) The 3D posterior view of the liver. (d) The 3D anterior view of the liver where the seven liver portions and the vein are made semi-transparent to visualize the 2.11 mm<sup>3</sup> positioned spheric tumor in the lobus dexter medialis. 1=lobus sinister lateralis, 2=lobus dexter medialis, 3=processus caudatus, 4=lobus sinister medialis, 5=lobus dexter lateralis, 6=processus papillaris I, 7=processus papillaris II, a = esophagus and b = vein.

lateralis, lobus dexter medialis, processus caudatus, lobus sinister medialis, lobus dexter lateralis, processus papillaris I, and processus papillaris II) according to published atlases of rat anatomy (Fig. 2).<sup>39,44</sup> The number of voxels of each identified region is then calculated and multiplied by the voxel volume (0.1 × 0.1 × 0.1 mm<sup>3</sup>) and tissue density to yield the region mass. Table I shows the masses of the seven identified liver regions, the blood in the liver, and the total liver of this rat model as well as liver masses of other computational rat models.<sup>34,37,45</sup> In general, the mass of the liver is linked to the age of the rat. The elder rats are heavier than young rats and have higher liver mass. Figure 2 shows the original and seg-

TABLE I. Masses of identified liver lobes in the present rat model and values reported in related studies.

Organ/tissue	Mass (g)
Lobus sinister lateralis	2.08
Lobus dexter medialis	1.93
Processus caudatus	0.69
Lobus sinister medialis	0.48
Lobus dexter lateralis	0.72
Processus papillaris I	0.36
Processus papillaris II	0.39
Blood in the liver	0.54
Total liver	6.65
Liver of 248g rat (Ref. 37)	9.64
Liver of 310g rat (Ref. 34)	11.68
Liver of 386g rat (Ref. 45)	21.90

mented images on a slice at the level of the abdomen of the rat model and the anterior and posterior views of the liver region. To evaluate dose volume distributions for different radionuclides in the liver tumor and surrounding normal tissues, a spherical hepatic tumor<sup>46</sup> with a volume of 2.11 mm<sup>3</sup> was positioned in the lobus dexter medialis [Fig. 2(d)].

The densities of organs were assumed to be consistent with those recommended for humans. In the absence of well-established animal data, except for the liver, tissue chemical compositions recommended for humans<sup>47,48</sup> were used for corresponding tissues of the rat model. In the seven identified liver regions (medium 1), tissue composition data (Na, K, Mg, P, and Fe) were taken from Cockell *et al.*<sup>39</sup> whereas the proportions of H, C, N, O and Cl were assumed to be consistent with soft tissue analog reported in the Medical Internal Radiation Dose Committee (MIRD) Pamphlet 8.<sup>32</sup> Let us assume that the chemical fractions of Na, K, P, Mg, and Fe measured by Cockell *et al.* are  $C_{Na}$ ,  $C_K$ ,  $C_P$ ,  $C_{Mg}$ , and  $C_{Fe}$ , and the chemical fractions of H, C, N, O, and Cl in the MIRD soft tissue analog are  $P_H$ ,  $P_C$ ,  $P_N$ ,  $P_O$ , and  $P_{Cl}$ , respectively. The chemical compositions of the seven lobes were obtained by

$$R_H = \frac{[1 - (C_{Na} + C_P + C_K + C_{Mg} + C_{Fe})]}{P_H + P_C + P_N + P_O + P_{Cl}} \times P_H,$$

$$R_C = \frac{[1 - (C_{Na} + C_P + C_K + C_{Mg} + C_{Fe})]}{P_H + P_C + P_N + P_O + P_{Cl}} \times P_C,$$

$$R_N = \frac{[1 - (C_{Na} + C_P + C_K + C_{Mg} + C_{Fe})]}{P_H + P_C + P_N + P_O + P_{Cl}} \times P_N,$$

$$R_O = \frac{[1 - (C_{Na} + C_P + C_K + C_{Mg} + C_{Fe})]}{P_H + P_C + P_N + P_O + P_{Cl}} \times P_O,$$

$$R_{Cl} = \frac{[1 - (C_{Na} + C_P + C_K + C_{Mg} + C_{Fe})]}{P_H + P_C + P_N + P_O + P_{Cl}} \times P_{Cl},$$

$$R_{Na} = C_{Na},$$

$$R_{Mg} = C_{Mg},$$

$$R_{Fe} = C_{Fe},$$

$$R_P = C_P,$$

$$R_K = P_K,$$

where  $R_H$ ,  $R_C$ ,  $R_N$ ,  $R_O$ ,  $R_{Cl}$ ,  $R_{Na}$ ,  $R_{Mg}$ ,  $R_{Fe}$ ,  $R_P$ , and  $R_K$  refer to the chemical fractions of H, C, N, O, Cl, Na, Mg, Fe, P, and K in the liver lobes.

The composition of tumor tissue is mixed from the major element compositions of the MIRD soft tissue analog and the trace element compositions of secondary liver tumors reported in the literature.<sup>46</sup>

To estimate the effect of chemical composition on rat organ radiation dose calculation, Monte Carlo simulations were also performed using two different arrangements by changing the chemical composition of the voxel filling material in the liver using the ICRU recommended human tissue (medium 2)<sup>47,49</sup> and MIRD defined soft tissue analog (medium 3).<sup>32</sup> Table II shows the adopted chemical compositions of different liver lobes and simulated liver tumor in this

TABLE II. Comparison of chemical compositions of identified liver lobes in this work and those recommended for humans.

Tissue		Chemical compositions											
		H	C	N	O	Na	P	S	Cl	K	Mg	Fe	Zn
Mixture: MIRD Soft Tissue	Lobus sinister lateralis	9.94	14.8	3.45	70.93	0.06 <sup>a</sup>	0.33 <sup>a</sup>	-	0.1	0.36 <sup>a</sup>	0.02 <sup>a</sup>	0.01 <sup>a</sup>	-
Analog + Liver Rat <sup>a</sup>	Lobus dexter medialis	9.94	14.8	3.45	70.94	0.05 <sup>a</sup>	0.34 <sup>a</sup>	-	0.1	0.35 <sup>a</sup>	0.02 <sup>a</sup>	0.01 <sup>a</sup>	-
	Processus caudatus	9.94	14.8	3.45	70.95	0.06 <sup>a</sup>	0.32 <sup>a</sup>	-	0.1	0.35 <sup>a</sup>	0.02 <sup>a</sup>	0.01 <sup>a</sup>	-
	Lobus sinister medialis	9.94	14.8	3.45	70.93	0.06 <sup>a</sup>	0.34 <sup>a</sup>	-	0.1	0.36 <sup>a</sup>	0.02 <sup>a</sup>	0.01 <sup>a</sup>	-
	Lobus dexter lateralis	9.94	14.8	3.45	70.94	0.06 <sup>a</sup>	0.33 <sup>a</sup>	-	0.1	0.35 <sup>a</sup>	0.02 <sup>a</sup>	0.01 <sup>a</sup>	-
	Processus papillaris	9.94	14.8	3.45	70.95	0.06 <sup>a</sup>	0.32 <sup>a</sup>	-	0.1	0.35 <sup>a</sup>	0.02 <sup>a</sup>	0.01 <sup>a</sup>	-
ICRU 44 liver adult		10.2	13.9	3.0	71.6	0.2	0.3	0.3	0.2	0.3	-	-	-
MIRD soft tissue analog		10.0	14.89	3.47	71.39	0.15	-	-	0.1	-	-	-	-
Mixture: MIRD soft tissue analog + secondary liver tumor <sup>b</sup>		9.99	14.87	3.47	71.31	0.15	-	-	0.1	-	-	0.01 <sup>b</sup>	0.1 <sup>b</sup>

<sup>a</sup>Chemical compositions reported by Cockell *et al.* (Ref. 39).

<sup>b</sup>Trace element compositions of secondary liver tumor given by Gurusamy *et al.* (Ref. 46).

work as compared to values recommended for human liver and the MIRD soft tissue analog.

## II.B. Calculations of dosimetric quantities

The most commonly used internal dose estimation schema devised by the MIRD Committee was adopted in this work for the calculation of the mean absorbed dose, defined as the product of the cumulated activity and the radionuclide S-value<sup>50</sup>:

$$D(r_T, T_D) = \int_0^{T_D} \dot{D}(r_T, t) dt = \sum_{r_S} \int_0^{T_D} A(r_S, t) S(r_T \leftarrow r_S) dt, \quad (1)$$

where  $D(r_T, T_D)$  is the mean absorbed dose to a given target organ  $r_T$  from radiation emitted from source organ  $r_S$  over a defined dose-integration period  $T_D$ .  $A(r_S, t)$  is the time-dependent activity of the radiopharmaceutical in source organ  $r_S$ .  $S(r_T \leftarrow r_S)$  is the S-value describing the equivalent dose rate in the target organ per unit activity in the source organ.<sup>50,51</sup> S-values are dependent on the characteristics of the radionuclide and the anatomic specifications of the computational model from which it is calculated. For a specific radionuclide, the S-value is given by:

$$\begin{aligned} S(r_T \leftarrow r_S) &= \frac{1}{M(r_T)} \sum_i E_i Y_i \phi(r_T \leftarrow r_S, E_i) \\ &= \sum_i \Delta_i \Phi(r_T \leftarrow r_S, E_i), \end{aligned} \quad (2)$$

where  $Y_i$  is the average number of the  $i$ th radiation type particles emitted from the source region per nuclear transition (in  $\text{Bq}^{-1} \text{s}^{-1}$ ),  $M(r_T)$  is the mass of target organ  $t$  (in grams),  $\phi(r_T \leftarrow r_S, E_i)$  and  $\Phi(r_T \leftarrow r_S, E_i)$  are, respectively, the absorbed fraction (AF) and specific absorbed fraction (SAF) of radiation energy  $E_i$  in the target organ  $r_T$  for the  $i$ th radiation type originating in the source organ  $r_S$ . The AF describes the proportion of energy deposited in the target organ, also termed the self-AF when the target organ is the source organ. The SAF describes the mean absorbed fraction in a target organ and is given as the ratio of the absorbed fraction and the target mass.

## II.C. Monte Carlo simulations

MCNPX, an extensively benchmarked multiparticle Monte Carlo radiation transport code,<sup>52</sup> is adopted in this study to simulate radiation transport of photons and electrons in the voxel-based rat model. In the absorbed dose estimations, the left kidney, right kidney, lungs, spleen, stomach, esophagus, and blood are only selected as internal sources, and the seven identified liver lobes are all used as both target and source regions. For comparison with published results, photon and electron sources were assumed to be uniformly distributed throughout 14 chosen source regions. Monoenergetic photons and electrons were generated from the source organs with 24 selected energy values ranging from 0.01 to 4.0 MeV and 0.1 to 5.0 MeV, respectively. The MCPLIB02 data library for photon transport and the default electron transport algorithm were adopted in the simulations. Photons were fully transported, while a cutoff energy of 10 keV was set for secondary electrons to speed up the simulations without compromising the accuracy of energy deposition estimation. A total of  $3.0 \times 10^7$  primary particle histories (NPS) are generated such that the statistical uncertainties of the results are less than 2%.

To evaluate the voxel S-values in the liver lobes and compare the results to reference values reported in MIRD pamphlet 17,<sup>53</sup> the EGS-based DOSXYZnrc Monte Carlo code<sup>54</sup> was used to perform radiation transport simulation and energy deposited in each voxel of the rat model where a voxel source is situated at the center of the added tumor. To evaluate the dose distribution from radioactive microspheres in the tumor, lobe, and total liver, a voxel source with a size of  $100 \times 100 \times 100 \mu\text{m}$ , close to the size of radioactive microspheres used in radionuclide therapy research,<sup>15,17</sup> is simulated. The photon and electron production and transport thresholds in DOSXYZnrc simulations were set to  $\text{PCUT} = 0.001 \text{ MeV}$  and  $\text{ECUT} = 0.512 \text{ MeV}$ , respectively. The number of particles simulated in the DOSXYZnrc is  $1.0 \times 10^9$ . With respect to the energy range of photons and electrons emitted from typical radionuclides, voxel absorbed fractions for monoenergetic electron sources with energies ranging from 0.1 to 1.0 MeV and photon sources with

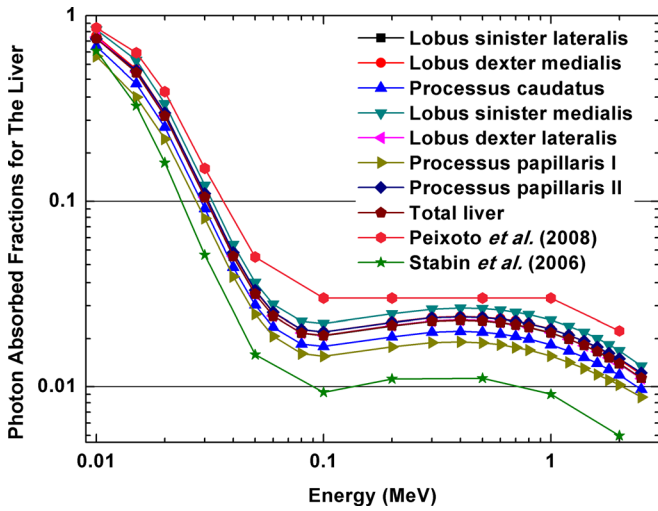


FIG. 3. Photon absorbed fractions for the total liver region with sources placed in the seven liver lobes and total liver and comparison with the results of Stabin *et al.* (Ref. 37) and Peixoto *et al.* (Ref. 34).

energies ranging from 0.01 to 2.5 MeV are obtained and used in the calculations of voxel S-values.

The MCNPX and DOSXYZnrc simulations are performed on four HP workstations (2 × 2.27 GHz Intel Xeon E5520, 24 GB RAM) under Microsoft Windows™ Vista operating system.

III. RESULTS

III.A. AF and SAF for rat liver

Figure 3 shows photon absorbed fractions for the total liver region with sources placed in each of the seven liver lobes. Comparison with the results of Stabin *et al.*<sup>37</sup> and Peixoto *et al.*<sup>34</sup> are also given. The AF curves in this figure first present sharp decrease when photon energy is below 0.1 MeV and then moderately rise to a local maximum at 0.4 MeV. After these local maximum values, the AF lines follow

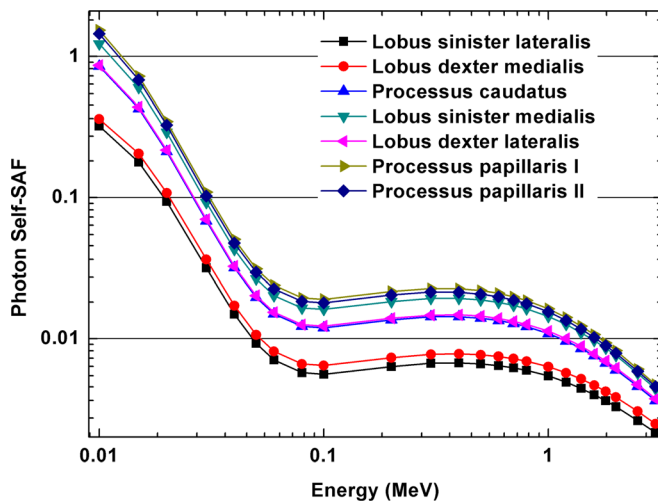
a gradual reduction, which indicates that raising photon energy facilitates the escape of recoil electron and scattered photons from the source organ.

Figure 4 shows the self-absorbed photon and electron SAF for the identified portions of the liver. For monoenergetic particles, the lobus sinister lateralis and the lobus dexter medialis yield the lowest SAFs, whereas the processus caudatus and the lobus sinister medialis display a medium SAF, and the lobus sinister medialis and processus papillaris I and II give the highest SAF values.

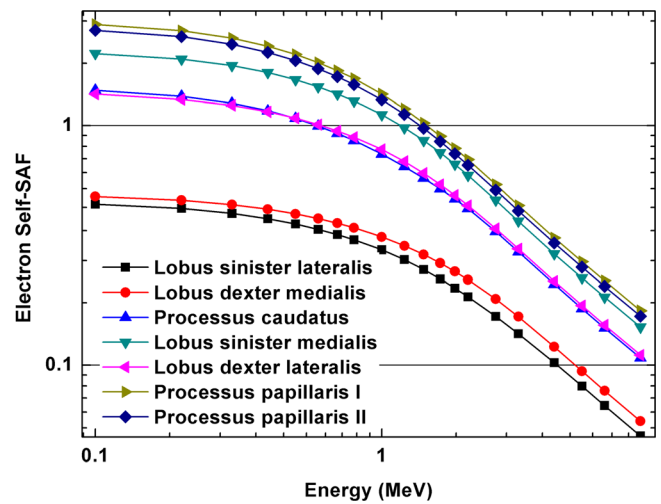
Figure 5 illustrates the absorbed fraction proportions of the liver regions to that of the combined liver when photon emitting sources are placed in the left kidney, the right kidney, the lung, and the stomach, respectively. For a photon source in the left kidney and the stomach, the processus caudatus and the lobus sinister lateralis contribute to more than 40% of the liver averaged dose. When the lung is set as the source organ, most liver dose (>80%) is deposited in the lobus sinister lateralis, the lobus dexter medialis, and the lobus dexter lateralis. With the right kidney as source organ, the lobus sinister lateralis and processus papillaris I receive more than half of the liver dose.

III.B. Effect of chemical composition in rat liver dose estimation

Figure 6 compares self-absorbed fractions for the total liver versus the chemical composition of the liver defined as rat tissue (medium 1), human tissue (medium 2), and soft tissue analog (medium 3), when the lobus dexter medialis is set as the source region. As shown in Fig. 6(a), at an emitting photon energy of 30 keV, the maximum percentage difference of self-AF for the total liver between media 2 and 1 is 3.5%, while this difference is -9.8% between media 3 and 1. The percentage differences of electron absorbed fractions for the liver for these three media are all below 0.5% for each energy.



(a)



(b)

FIG. 4. (a) Photon and (b) electron self-absorbed SAF for the seven lobes of liver of the rat phantom.

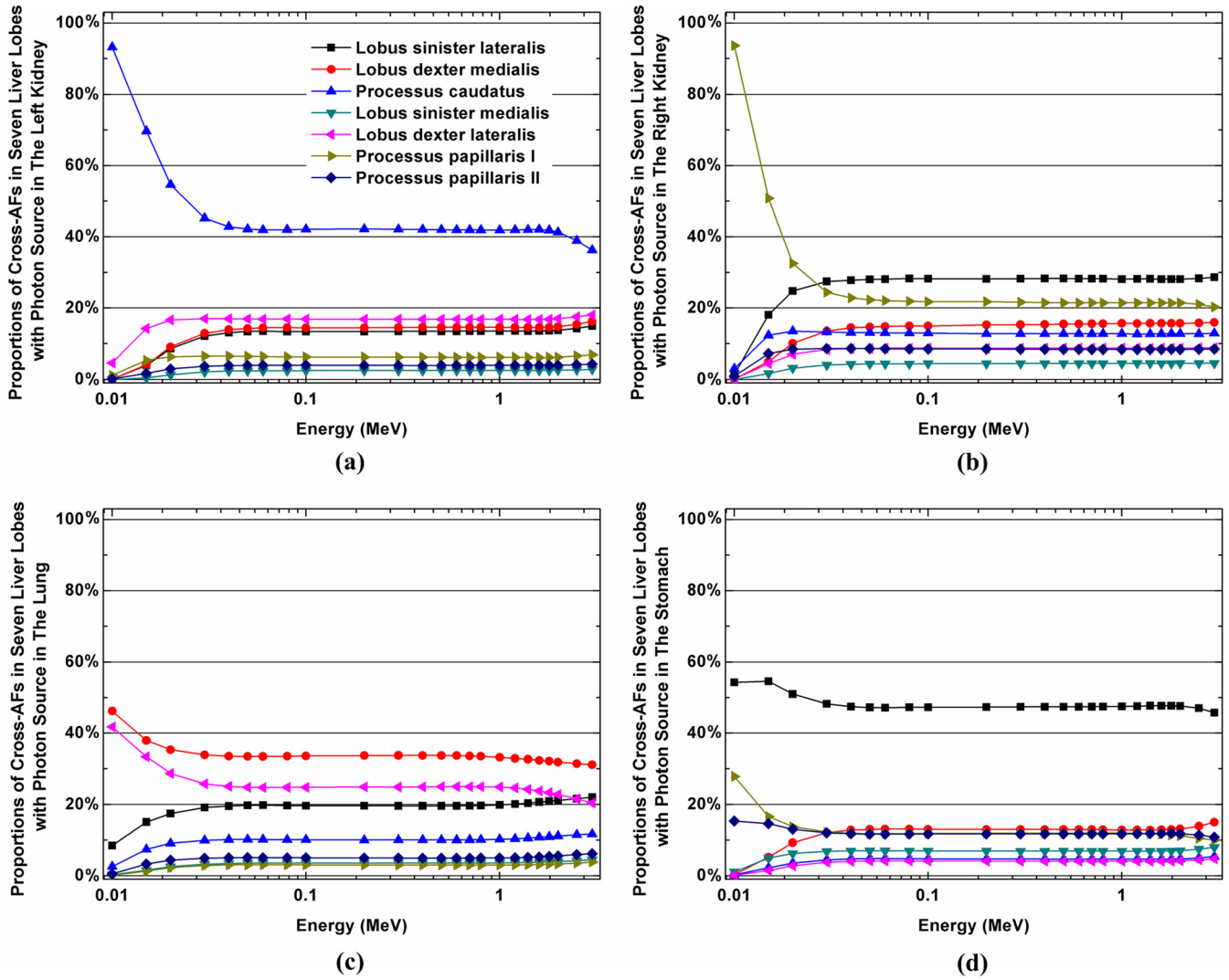


FIG. 5. The absorbed fraction proportions of the seven identified liver regions with photon emitting sources localized in (a) the left kidney, (b) the right kidney, (c) the lung, and (d) the stomach.

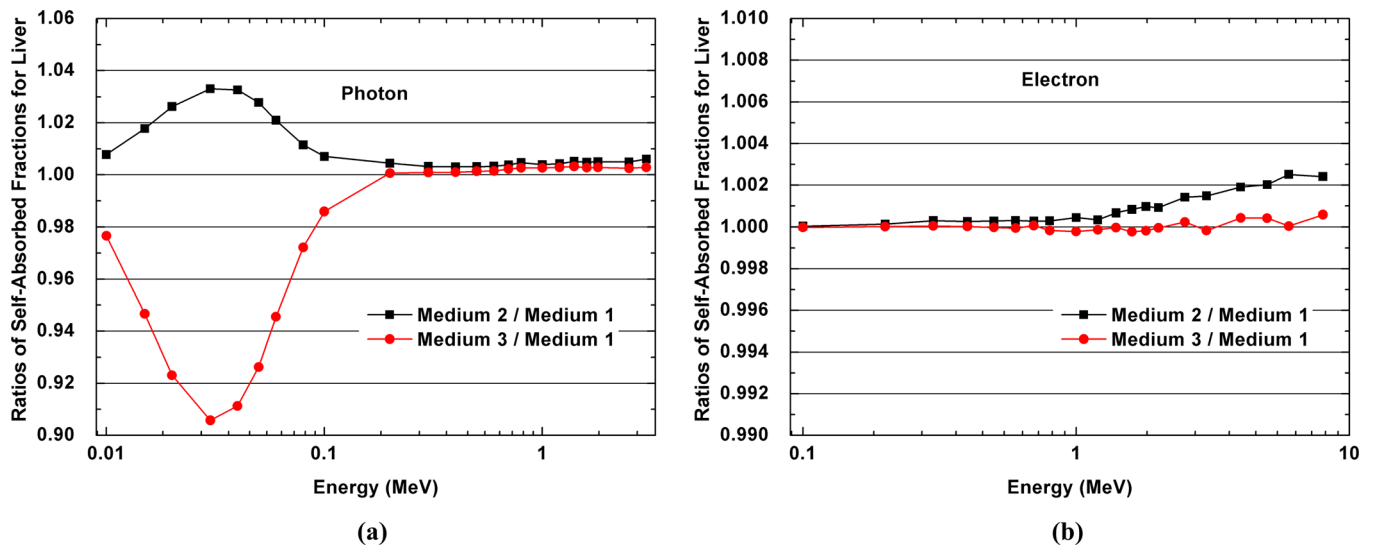


FIG. 6. Comparison of the self-absorbed fractions for the combined liver, when the (a) photon and (b) electron emitting source is placed in the lobus dexter medialis, with the chemical compositions of liver defined as rat tissue (medium 1), human tissue (medium 2), and soft tissue analog (medium 3), respectively. The results are shown as ratios of liver absorbed fractions of human tissue (medium 2) and soft tissue analog (medium 3) to that of rat tissue (medium 1).

**III.C. S-values and dose-volume histograms (DVHs) for radionuclides**

Based on the absorbed fractions calculated from MCNPX simulations, S-values of <sup>131</sup>I, <sup>90</sup>Y, <sup>188</sup>Re, and <sup>166</sup>Ho for the liver lobes and the blood in the liver of the rat model are summarized in Table III. The results of this work suggest that the lobus sinister lateralis receives the lowest self-absorbed S-values for <sup>131</sup>I [ $1.46 \times 10^{-02}$  mGy/(MBq s)], <sup>90</sup>Y [ $6.66 \times 10^{-02}$  mGy/(MBq s)], and <sup>166</sup>Ho [ $9.86 \times 10^{-02}$  mGy/(MBq s)]. The processus papillaris II gives the highest self-absorbed S-values for <sup>90</sup>Y [ $2.65 \times 10^{-01}$  mGy/(MBq s)], <sup>188</sup>Re [ $2.48 \times 10^{-01}$  mGy/(MBq s)], and <sup>166</sup>Ho [ $4.76 \times 10^{-01}$  mGy/(MBq s)]. Table IV compares the self-absorbed S-values for the total liver of different rat models. It is noticed that the S-values for the livers are inversely proportional to the liver mass. By using the mass-based correction

method,<sup>51,55</sup> S-values calculated in this work could be applied to the rats of different masses and sizes.

The voxel S-values obtained using DOSXYZnrc simulations are shown in Figs. 7 and 8. Figure 7 shows the isodose curves for the considered radionuclides in the latitudinal plane of the liver with voxel source placed at the center of the tumor, and the 1%, 2%, 5%, 10%, 20%, 50%, 100%, and 300% isodose curves pictured on top of a grayscale image illustrating the liver region. In general, the DVH is the most common way to visualize the absorbed dose distribution within a volume of interest. For an average tumor dose of 100 Gy, the DVHs of the tumor and the lobus dexter medialis for <sup>90</sup>Y, <sup>131</sup>I, <sup>166</sup>Ho, and <sup>188</sup>Re voxel sources placed at the center of the tumor are displayed in Fig. 8. The almost rectangular shaped DVH curves observed for <sup>90</sup>Y, <sup>166</sup>Ho, and <sup>188</sup>Re for the tumor suggest a uniform absorbed dose

TABLE III. S-values for <sup>131</sup>I, <sup>90</sup>Y, <sup>188</sup>Re, and <sup>166</sup>Ho for the seven liver lobes and the blood in the liver of the rat model.

Target tissue	Source tissue							
	Lobus sinister lateralis	Lobus dexter medialis	Processus caudatus	Lobus sinister medialis	Lobus dexter lateralis	Processus papillaris I	Processus papillaris II	Total liver
<b><sup>131</sup>I mGy/(MBq s)</b>								
Lobus sinister lateralis	$1.36 \times 10^{-02}$	$1.62 \times 10^{-04}$	$7.01 \times 10^{-05}$	$6.12 \times 10^{-04}$	$9.20 \times 10^{-05}$	$9.16 \times 10^{-05}$	$6.39 \times 10^{-04}$	$4.39 \times 10^{-03}$
Lobus dexter medialis	$1.61 \times 10^{-04}$	$1.47 \times 10^{-02}$	$7.97 \times 10^{-05}$	$5.11 \times 10^{-04}$	$3.47 \times 10^{-04}$	$4.79 \times 10^{-05}$	$7.72 \times 10^{-05}$	$4.40 \times 10^{-03}$
Processus caudatus	$6.92 \times 10^{-05}$	$8.05 \times 10^{-05}$	$3.97 \times 10^{-02}$	$4.41 \times 10^{-05}$	$8.76 \times 10^{-04}$	$1.48 \times 10^{-04}$	$2.74 \times 10^{-04}$	$4.29 \times 10^{-03}$
Lobus sinister medialis	$6.05 \times 10^{-04}$	$5.10 \times 10^{-04}$	$4.40 \times 10^{-05}$	$5.67 \times 10^{-02}$	$5.87 \times 10^{-05}$	$5.76 \times 10^{-05}$	$1.04 \times 10^{-04}$	$4.47 \times 10^{-03}$
Lobus dexter lateralis	$9.22 \times 10^{-05}$	$3.46 \times 10^{-04}$	$8.73 \times 10^{-04}$	$5.91 \times 10^{-05}$	$3.86 \times 10^{-02}$	$8.04 \times 10^{-05}$	$1.17 \times 10^{-04}$	$4.39 \times 10^{-03}$
Processus papillaris I	$9.17 \times 10^{-05}$	$4.88 \times 10^{-05}$	$1.49 \times 10^{-04}$	$5.67 \times 10^{-05}$	$8.10 \times 10^{-05}$	$7.43 \times 10^{-02}$	$4.93 \times 10^{-04}$	$4.21 \times 10^{-03}$
Processus papillaris II	$6.37 \times 10^{-04}$	$7.82 \times 10^{-05}$	$2.71 \times 10^{-04}$	$1.06 \times 10^{-04}$	$1.16 \times 10^{-04}$	$4.93 \times 10^{-04}$	$7.02 \times 10^{-02}$	$4.36 \times 10^{-03}$
Total liver	$4.39 \times 10^{-03}$	$4.41 \times 10^{-03}$	$4.27 \times 10^{-03}$	$4.49 \times 10^{-03}$	$4.38 \times 10^{-03}$	$4.18 \times 10^{-03}$	$4.36 \times 10^{-03}$	$4.37 \times 10^{-03}$
<b><sup>90</sup>Y mGy/(MBq s)</b>								
Lobus sinister lateralis	$4.67 \times 10^{-02}$	$1.96 \times 10^{-03}$	$4.05 \times 10^{-04}$	$1.11 \times 10^{-02}$	$6.34 \times 10^{-04}$	$4.05 \times 10^{-06}$	$1.20 \times 10^{-02}$	$1.68 \times 10^{-02}$
Lobus dexter medialis	$1.96 \times 10^{-03}$	$5.27 \times 10^{-02}$	$9.02 \times 10^{-05}$	$9.39 \times 10^{-03}$	$5.66 \times 10^{-03}$	$6.46 \times 10^{-07}$	$1.48 \times 10^{-05}$	$1.72 \times 10^{-02}$
Processus caudatus	$4.06 \times 10^{-04}$	$9.05 \times 10^{-05}$	$1.19 \times 10^{-01}$	$3.22 \times 10^{-06}$	$1.64 \times 10^{-02}$	$1.76 \times 10^{-03}$	$4.02 \times 10^{-03}$	$1.46 \times 10^{-02}$
Lobus sinister medialis	$1.11 \times 10^{-02}$	$9.38 \times 10^{-03}$	$3.08 \times 10^{-06}$	$1.74 \times 10^{-01}$	$4.26 \times 10^{-05}$	$7.48 \times 10^{-07}$	$2.33 \times 10^{-06}$	$1.88 \times 10^{-02}$
Lobus dexter lateralis	$6.29 \times 10^{-04}$	$5.68 \times 10^{-03}$	$1.63 \times 10^{-02}$	$4.27 \times 10^{-05}$	$1.24 \times 10^{-01}$	$1.29 \times 10^{-06}$	$6.49 \times 10^{-04}$	$1.69 \times 10^{-02}$
Processus papillaris I	$3.60 \times 10^{-06}$	$6.31 \times 10^{-07}$	$1.76 \times 10^{-03}$	$7.24 \times 10^{-07}$	$1.23 \times 10^{-06}$	$2.13 \times 10^{-01}$	$7.95 \times 10^{-03}$	$1.24 \times 10^{-02}$
Processus papillaris II	$1.20 \times 10^{-02}$	$1.34 \times 10^{-05}$	$4.01 \times 10^{-03}$	$2.23 \times 10^{-06}$	$6.52 \times 10^{-04}$	$7.83 \times 10^{-03}$	$2.01 \times 10^{-01}$	$1.63 \times 10^{-02}$
Total liver	$1.68 \times 10^{-02}$	$1.72 \times 10^{-02}$	$1.45 \times 10^{-02}$	$1.88 \times 10^{-02}$	$1.69 \times 10^{-02}$	$1.23 \times 10^{-02}$	$1.63 \times 10^{-02}$	$1.65 \times 10^{-02}$
<b><sup>188</sup>Re mGy/(MBq s)</b>								
Lobus sinister lateralis	$4.12 \times 10^{-02}$	$1.33 \times 10^{-03}$	$2.83 \times 10^{-04}$	$7.94 \times 10^{-03}$	$4.63 \times 10^{-04}$	$1.76 \times 10^{-05}$	$8.58 \times 10^{-03}$	$1.44 \times 10^{-02}$
Lobus dexter medialis	$1.33 \times 10^{-03}$	$4.62 \times 10^{-02}$	$7.48 \times 10^{-05}$	$6.67 \times 10^{-03}$	$4.01 \times 10^{-03}$	$8.95 \times 10^{-06}$	$1.62 \times 10^{-05}$	$1.47 \times 10^{-02}$
Processus caudatus	$2.83 \times 10^{-04}$	$7.50 \times 10^{-05}$	$1.08 \times 10^{-01}$	$8.96 \times 10^{-06}$	$1.17 \times 10^{-02}$	$9.55 \times 10^{-04}$	$2.78 \times 10^{-03}$	$1.28 \times 10^{-02}$
Lobus sinister medialis	$7.88 \times 10^{-03}$	$6.66 \times 10^{-03}$	$8.71 \times 10^{-06}$	$1.57 \times 10^{-01}$	$3.81 \times 10^{-05}$	$1.07 \times 10^{-05}$	$1.98 \times 10^{-05}$	$1.58 \times 10^{-02}$
Lobus dexter lateralis	$4.61 \times 10^{-04}$	$4.03 \times 10^{-03}$	$1.16 \times 10^{-02}$	$3.77 \times 10^{-05}$	$1.11 \times 10^{-01}$	$1.51 \times 10^{-05}$	$4.07 \times 10^{-04}$	$1.45 \times 10^{-02}$
Processus papillaris I	$1.76 \times 10^{-05}$	$8.97 \times 10^{-06}$	$9.61 \times 10^{-04}$	$1.04 \times 10^{-05}$	$1.51 \times 10^{-05}$	$1.96 \times 10^{-01}$	$5.32 \times 10^{-03}$	$1.12 \times 10^{-02}$
Processus papillaris II	$8.57 \times 10^{-03}$	$1.61 \times 10^{-05}$	$2.76 \times 10^{-03}$	$2.01 \times 10^{-05}$	$4.10 \times 10^{-04}$	$5.23 \times 10^{-03}$	$1.84 \times 10^{-01}$	$1.40 \times 10^{-02}$
Total liver	$1.44 \times 10^{-02}$	$1.47 \times 10^{-02}$	$1.27 \times 10^{-02}$	$1.59 \times 10^{-02}$	$1.45 \times 10^{-02}$	$1.12 \times 10^{-02}$	$1.40 \times 10^{-02}$	$1.42 \times 10^{-02}$
<b><sup>166</sup>Ho mGy/(MBq s)</b>								
Lobus sinister lateralis	$7.60 \times 10^{-02}$	$2.03 \times 10^{-03}$	$4.54 \times 10^{-04}$	$1.24 \times 10^{-02}$	$7.59 \times 10^{-04}$	$6.64 \times 10^{-05}$	$1.35 \times 10^{-02}$	$2.61 \times 10^{-02}$
Lobus dexter medialis	$2.03 \times 10^{-03}$	$8.47 \times 10^{-02}$	$1.52 \times 10^{-04}$	$1.04 \times 10^{-02}$	$6.27 \times 10^{-03}$	$3.23 \times 10^{-05}$	$5.46 \times 10^{-05}$	$2.66 \times 10^{-02}$
Processus caudatus	$4.52 \times 10^{-04}$	$1.53 \times 10^{-04}$	$2.02 \times 10^{-01}$	$3.01 \times 10^{-05}$	$1.82 \times 10^{-02}$	$1.25 \times 10^{-03}$	$4.27 \times 10^{-03}$	$2.35 \times 10^{-02}$
Lobus sinister medialis	$1.23 \times 10^{-02}$	$1.04 \times 10^{-02}$	$2.99 \times 10^{-05}$	$2.95 \times 10^{-01}$	$7.86 \times 10^{-05}$	$3.88 \times 10^{-05}$	$7.49 \times 10^{-05}$	$2.82 \times 10^{-02}$
Lobus dexter lateralis	$7.54 \times 10^{-04}$	$6.30 \times 10^{-03}$	$1.81 \times 10^{-02}$	$7.87 \times 10^{-05}$	$2.07 \times 10^{-01}$	$5.72 \times 10^{-05}$	$6.25 \times 10^{-04}$	$2.62 \times 10^{-02}$
Processus papillaris I	$6.68 \times 10^{-05}$	$3.24 \times 10^{-05}$	$1.26 \times 10^{-03}$	$3.84 \times 10^{-05}$	$5.70 \times 10^{-05}$	$3.70 \times 10^{-01}$	$8.04 \times 10^{-03}$	$2.11 \times 10^{-02}$
Processus papillaris II	$1.34 \times 10^{-02}$	$5.47 \times 10^{-05}$	$4.22 \times 10^{-03}$	$7.62 \times 10^{-05}$	$6.23 \times 10^{-04}$	$7.91 \times 10^{-03}$	$3.49 \times 10^{-01}$	$2.54 \times 10^{-02}$
Total liver	$2.61 \times 10^{-02}$	$2.67 \times 10^{-02}$	$2.34 \times 10^{-02}$	$2.84 \times 10^{-02}$	$2.62 \times 10^{-02}$	$2.10 \times 10^{-02}$	$2.54 \times 10^{-02}$	$2.58 \times 10^{-02}$

TABLE IV. Comparison of self-absorbed S-values for the total rat liver from the four radionuclides with those of published works.

	Liver mass (g)	S-values for the total liver ( $\times 10^{-02}$ mGy MBq $^{-1}$ s $^{-1}$ )			
		$^{131}\text{I}$	$^{90}\text{Y}$	$^{188}\text{Re}$	$^{166}\text{Ho}$
This work	6.65	0.44	1.65	1.42	2.58
248 g rat <sup>a</sup>	9.64	0.31	1.30	1.1	1.96
310 g rat <sup>b</sup>	11.68	0.26	1.08	0.91	1.64

<sup>a</sup>S-values calculated from the absorbed fractions reported by Stabin *et al.* (Ref. 37).

<sup>b</sup>S-values calculated from the absorbed fractions reported by Peixoto *et al.* (Ref. 34).

distribution in the volume. Nevertheless,  $^{131}\text{I}$  produces a relatively irregular DVH for the liver tumor of the rat model. In the case of  $^{90}\text{Y}$ ,  $^{166}\text{Ho}$ , and  $^{188}\text{Re}$ , most tissue regions within the tumor receive absorbed doses ranging from 24 to 500 Gy, while only a small percentage (<1%) of the tumor receive a dose above 500 Gy. For  $^{131}\text{I}$ , the voxel absorbed doses show an irregular distribution in the tumor region where 72% of the tumor volume receives less than 1 Gy and 10% of the tumor volume receives above 200 Gy. A fairly uniform dose distribution in the lobus dexter medialis region is also observed.  $^{90}\text{Y}$  produce relatively higher doses for the surrounding normal tissue (10% lobus dexter medialis

volume receives over 0.3 Gy). The absorbed doses for  $^{131}\text{I}$ ,  $^{166}\text{Ho}$ , and  $^{188}\text{Re}$  are much lower: 10% of the volume receives over 0.008, 0.004, and 0.002 Gy for  $^{131}\text{I}$ ,  $^{166}\text{Ho}$ , and  $^{188}\text{Re}$ , respectively.

The MIRD pamphlet 17 (Ref. 53) provided voxel S-values of  $^{131}\text{I}$  within an octant of  $10 \times 10 \times 10$  voxels, where the first entry indicates the source voxel located at  $(I, J, K) = (0, 0, 0)$  and the remaining entries represent the target voxels. S-values for other octants could be obtained by invoking symmetry arguments. The target region in MIRD17 was a water-filled cube with  $2 \times 2 \times 2$  mm $^3$  volume. If we select voxels in a sphere centered at the source voxel and having similar geometry as the simulated tumor, we obtain the modified DVH for  $^{131}\text{I}$  in water medium. Figure 9 compares the  $^{131}\text{I}$  DVH in the simulated tumor and the water medium. The differences between these DVHs are mainly caused by the different materials of the target regions.

#### IV. DISCUSSION

The self-AF curves of the total liver obtained in this work are comparable to AFs reported by Stabin *et al.*<sup>37</sup> and Pixoto *et al.*<sup>34</sup> (Fig. 3), and the self-AFs are susceptible to the location of the source in the liver. Currently, in most reported rat internal radiation dose studies, the liver is commonly assumed to be a homogeneous integrated target organ. In this work, the absorbed dose to suborgan regions of the liver are considered. The self-absorbed SAFs (Fig. 4) and self-irradiation S-values (Table III) present some differences among the seven liver regions. In most cases, the larger liver lobe yields a lower self-absorbed SAF and self-irradiation S-value. Meanwhile, the results shown in Table III demonstrate that, for certain radionuclides and source regions in the rat liver, the S-values for the source lobes, the target lobes and the total liver present significant differences. The S-value for the total liver is much higher than the values for target lobes but lower than that of the source lobe. According to Eq. (1), for a given activity of the radiopharmaceutical, when the S-value of the total liver is used to determine the absorbed dose to different liver regions, the dose to the source lobe will be underestimated while the dose to the target lobes would be significantly overestimated. At the same time, the cross-organ absorbed fractions (Fig. 5) for the liver region gives a nonuniform dose distribution among the different liver lobes depending on the distance between the source and target regions and the anatomical characteristics of different liver lobes.

In most published works, the chemical composition of rat tissues is usually assumed to be similar to that of humans, but this hypothesis might introduce additional errors when the results are used in rat internal dose estimations.<sup>56,57</sup> In this work, we quantify the influence of chemical composition using different media on rat liver absorbed fractions. The results demonstrate that variations in chemical composition (rat tissue vs human tissue) produce a maximum percentage difference for liver self-AF of 3.5% at photon energy of 30 keV whereas a minor effect is observed on the liver AFs for photon energies above 100 keV. Tissue

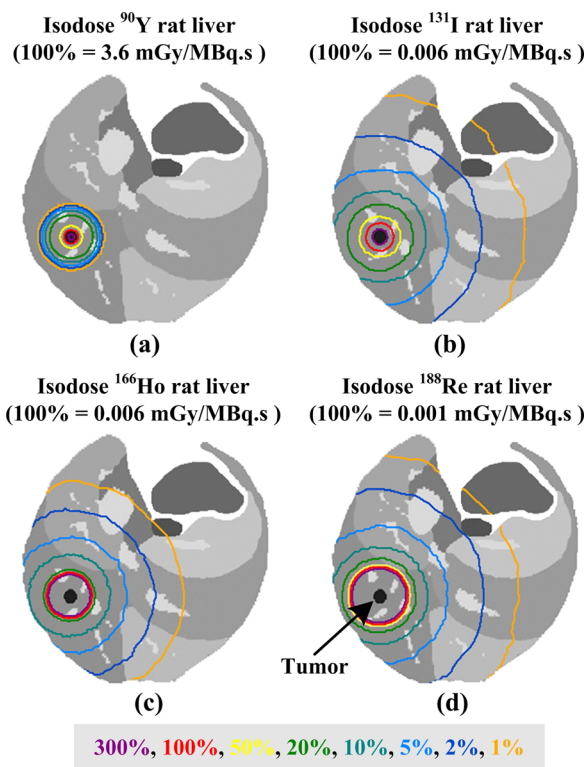


FIG. 7. Isodose curves for  $^{90}\text{Y}$  (a),  $^{131}\text{I}$  (b),  $^{166}\text{Ho}$  (c) and  $^{188}\text{Re}$  (d) in latitudinal plane of the liver are shown on top of a grayscale image describing the seven identified liver lobes, the vein, the esophagus, and the stomach of the rat phantom. The 1%, 2%, 5%, 10%, 20%, 50%, 100%, and 300% of isodose curves are indicated. The radionuclide sources are placed at the center of the 2.11 mm $^3$  tumor in the lobus dexter medialis.

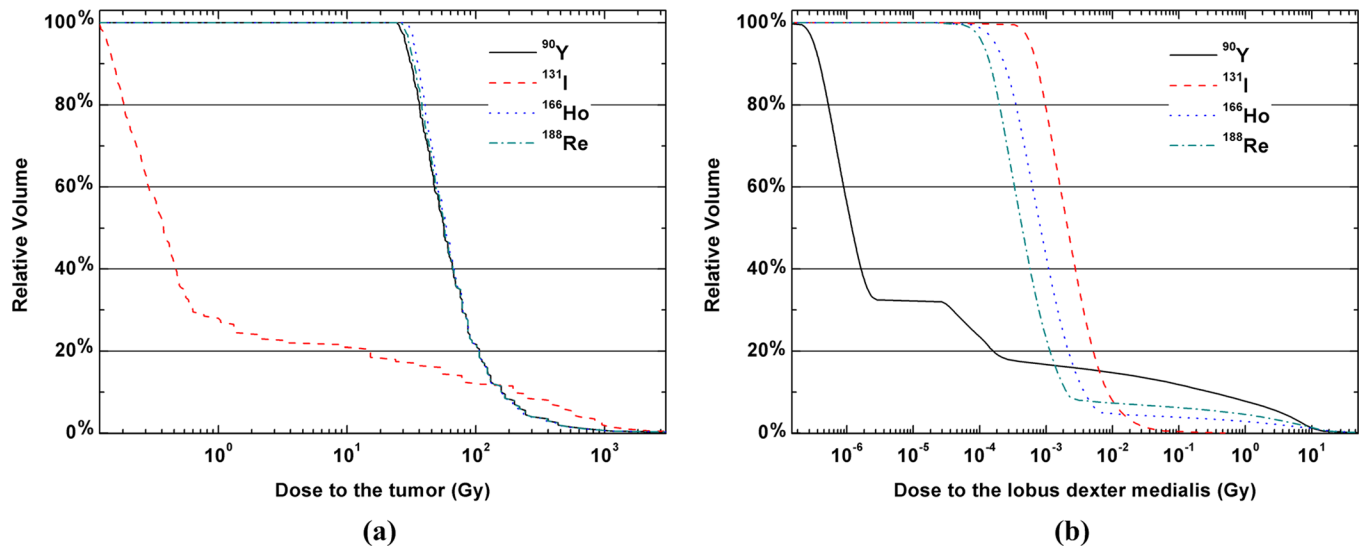


Fig. 8. Dose-volume histograms for (a) the tumor dose and (b) the lobus dexter medialis dose by activities of <sup>90</sup>Y, <sup>131</sup>I, <sup>166</sup>Ho, and <sup>188</sup>Re, which produce average dose to the tumor of 100 Gy, when placed in the center of the tumor.

composition differences result in negligible effects on electron absorbed dose.

With respect to the isodose curves shown in Fig. 7, slight differences in chemical composition between liver lobes do not produce observable effects on the voxel absorbed dose distributions. It is also interesting to note that in the photon energy range of 10–100 keV, the liver absorbed fractions of medium 3 are lower than those for media 1 and 2. The dominant interaction for photons in this energy range is photoelectric absorption, and the interaction cross section strongly depends on the atomic number of the absorber.<sup>58</sup> Therefore, since media 1 and 2 contain more elements with relatively high atomic numbers, more secondary electrons from photoelectric effect deposit more energy in the target region when increasing photon energy.

The DVHs and isodose curves for voxel absorbed dose illustrate that regions such as the lobus dexter medialis in the liver, which are close to the added tumor voxel source,

receive the largest absorbed dose. The distribution of voxel-absorbed dose presents a pattern depending on the radionuclide type. Meanwhile, since <sup>166</sup>Ho and <sup>188</sup>Re produce a uniform-distributed high dose in the tumor region and comparatively low absorbed dose for surrounding liver regions, we believe that radiopharmaceuticals and microspheres containing <sup>166</sup>Ho and <sup>188</sup>Re might be more effective and will have enormous clinical potential in radionuclide therapy of HCC.

In this work, we also evaluated the fractions of energy absorbed within the different microspheres from various radionuclides. In most cases, the photon and electron AFs in the microspheres were lower than 0.5% and 2%, respectively, except for β particles of <sup>131</sup>I and photons of <sup>166</sup>Ho in glass spheres. This is mainly due to the high density of glass spheres and the low average β particle energy of <sup>131</sup>I and low average photon energy of <sup>166</sup>Ho.

**V. CONCLUSION**

This study focused on the assessment of the absorbed dose to the rat liver using a new voxel-based rat model with identified suborgan liver regions through manual segmentation. Photon and electron AFs and radionuclide S-values for seven liver lobes demonstrate significant differences between self-absorbed SAFs and S-values with respect to the mass of liver lobes. Meanwhile, cross-organ absorbed doses yield nonuniform distributions throughout the liver. The results seem to suggest that, in rat liver radiation dose evaluations, when the radiolabeled microspheres are mostly concentrated in the lobe containing the tumor, the use of total liver S-values to determine the absorbed dose to different liver regions might underestimate the absorbed dose to the source lobe and overestimate it for other tissue regions. Therefore, it appears that, for absorbed dose calculation to rat liver for preclinical trials, it is important to consider the different lobes separately for accurate rat liver radiation dose calculation. It is suggested

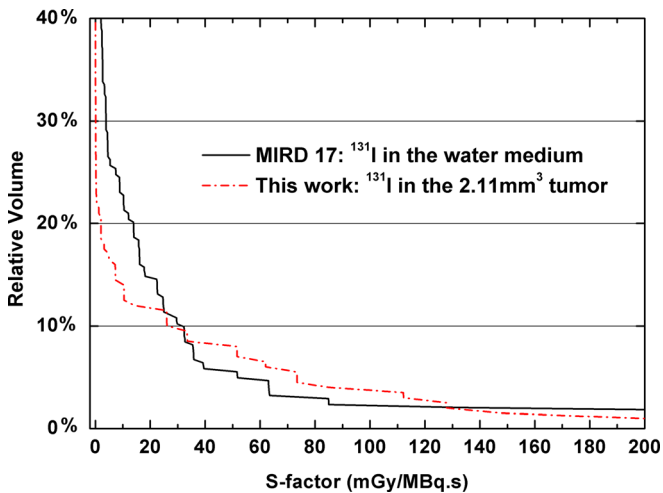


Fig. 9. Comparisons of <sup>131</sup>I DVH in 2.11 mm<sup>3</sup> tumor and the modified DVH for <sup>131</sup>I S-values provided by the MIRD pamphlet 17 (Ref. 53).

that detailed anatomical structures are important in organ-specific radiation dose calculations.

Consistent with clinical experience,<sup>59</sup> <sup>166</sup>Ho and <sup>188</sup>Re seem to be safer and more effective for radionuclide therapy of HCC compared to <sup>131</sup>I and <sup>90</sup>Y. The obtained results can be used to estimate the absorbed dose to the total liver and liver lobes separately, while the S-values can be used in research studies related to radionuclide therapy of HCC. The finer liver structures in the presented computational rat model offer the opportunity to improve the accuracy of rat liver radiation dose estimation. This work contributes to a better understanding of all aspects influencing radiation transport in organ-specific radiation dose evaluation for pre-clinical therapy studies, from tissue composition to organ morphology and activity distribution.

## ACKNOWLEDGMENTS

This work was supported by the National Natural Science Foundation of China (Grant No. 10875047), the Program for New Century Excellent Talents in University (Grant No. NCET-10-0386), the National Key Technology R&D Program 2011BAI12B03, the Swiss National Science Foundation under Grant No. SNSF 3152A0-102143, Geneva Cancer League, and the Indo-Swiss Joint Research Programme ISJRP 138866.

<sup>a)</sup>Author to whom correspondence should be addressed. Electronic mail: qianliu@mail.hust.edu.cn

- <sup>1</sup>I. M. Arias, W. B. Jakob, M. Popper, and D. Schachter, *The Liver—Biology and Pathobiology*, 2nd ed. (Raven Press, New York, 1988).
- <sup>2</sup>L. Miller, C. Bly, M. Watson, and W. Bale, "The dominant role of the liver in plasma protein synthesis," *J. Exp. Med.* **94**, 431–453 (1951).
- <sup>3</sup>J. C. Cheng *et al.*, "Radiation-induced liver disease after radiotherapy for hepatocellular carcinoma: clinical manifestation and dosimetric description," *Radiother. Oncol.* **63**, 41–45 (2002).
- <sup>4</sup>Y. Fong, R. L. Sun, W. Jarnagin, and L. H. Blumgart, "An analysis of 412 cases of hepatocellular carcinoma at a Western center," *Ann. Surg.* **229**, 790–799; discussion 799–800 (1999).
- <sup>5</sup>G. C. Cook, "Hepatocellular carcinoma: one of the world's most common malignancies," *Q. J. Med.* **57**, 705–708 (1985).
- <sup>6</sup>B. Lambert and C. Van de Wiele, "Treatment of hepatocellular carcinoma by means of radiopharmaceuticals," *Eur. J. Nucl. Med. Mol. Imaging* **32**, 980–989 (2005).
- <sup>7</sup>J. Raoul *et al.*, "Prospective randomized trial of chemoembolization versus intra-arterial injection of <sup>131</sup>I-labeled-iodized oil in the treatment of hepatocellular carcinoma," *Hepatology* **26**, 1156–1161 (1997).
- <sup>8</sup>J. L. Humm, "Dosimetric aspects of radiolabeled antibodies for tumor therapy," *J. Nucl. Med.* **27**, 1490–1497 (1986).
- <sup>9</sup>R. Salem *et al.*, "Use of Yttrium-90 glass microspheres (TheraSphere) for the treatment of unresectable hepatocellular carcinoma in patients with portal vein thrombosis," *J. Vasc. Interv. Radiol.* **15**, 335–345 (2004).
- <sup>10</sup>R. Salem, K. G. Thurston, B. I. Carr, J. E. Goin, and J. F. Geschwind, "Yttrium-90 microspheres: Radiation therapy for unresectable liver cancer," *J. Vasc. Interv. Radiol.* **13**, S223–S229 (2002).
- <sup>11</sup>W. A. Dezarn *et al.*, "Recommendations of the American Association of Physicists in Medicine on dosimetry, imaging, and quality assurance procedures for <sup>90</sup>Y microsphere brachytherapy in the treatment of hepatic malignancies," *Med. Phys.* **38**, 4824–4845 (2011).
- <sup>12</sup>G. J. Ehrhardt and D. E. Day, "Therapeutic use of <sup>90</sup>Y microspheres," *Int. J. Rad Appl. Instrum. B* **14**, 233–242 (1987).
- <sup>13</sup>A. Boschi *et al.*, "A kit formulation for the preparation of <sup>188</sup>Re-lipiodol: preclinical studies and preliminary therapeutic evaluation in patients with unresectable hepatocellular carcinoma," *Nucl. Med. Commun.* **25**, 691–699 (2004).
- <sup>14</sup>S. Wang *et al.*, "Biodistribution of rhenium-188 Lipiodol infused via the hepatic artery of rats with hepatic tumours," *Eur. J. Nucl. Med. Mol. Imaging* **23**, 13–17 (1996).
- <sup>15</sup>S. Wang *et al.*, "Intratymoral injection of rhenium-188 microspheres into an animal model of hepatoma," *J. Nucl. Med.* **39**, 1752–1757 (1998).
- <sup>16</sup>R. J. Mumper, U. Y. Ryo, and M. Jay, "Neutron-activated holmium-166-poly (L-lactic acid) microspheres: A potential agent for the internal radiation therapy of hepatic tumors," *J. Nucl. Med.* **32**, 2139–2143 (1991).
- <sup>17</sup>F. Nijssen *et al.*, "Targeting of liver tumour in rats by selective delivery of holmium-166 loaded microspheres: A biodistribution study," *Eur. J. Nucl. Med. Mol. Imaging* **28**, 743–749 (2001).
- <sup>18</sup>J. P. Geraci, K. L. Jackson, M. S. Mariano, and J. M. Leitch, "Hepatic injury after whole-liver irradiation in the rat," *Radiat. Res.* **101**, 508–518 (1985).
- <sup>19</sup>B. Jonsson, S. Strand, and B. Larsson, "A quantitative autoradiographic study of the heterogeneous activity distribution of different indium-111-labeled radiopharmaceuticals in rat tissues," *J. Nucl. Med.* **33**, 1825–1833 (1992).
- <sup>20</sup>E. Hindie, N. Colas-Linhart, A. Petiet, and B. Bok, "Microautoradiographic study of technetium-99m colloid uptake by the rat liver," *J. Nucl. Med.* **29**, 1118–1121 (1988).
- <sup>21</sup>J. S. Lewis, R. Laforest, M. R. Lewis, and C. J. Anderson, "Comparative dosimetry of copper-64 and yttrium-90-labeled somatostatin analogs in a tumor-bearing rat model," *Cancer. Biother. Radiopharm.* **15**, 593–604 (2000).
- <sup>22</sup>M. R. Mayberg, S. London, J. Rasey, and C. Gajdusek, "Inhibition of rat smooth muscle proliferation by radiation after arterial injury: Temporal characteristics in vivo and in vitro," *Radiat. Res.* **153**, 153–163 (2000).
- <sup>23</sup>D. K. Halford and O. D. Markham, "Radiation dosimetry of small mammals inhabiting a liquid radioactive waste disposal area," *Ecology* **59**, 1047–1054 (1978).
- <sup>24</sup>X. G. Xu and K. F. Eckerman, *Handbook of Anatomical Models for Radiation Dosimetry* (CRC Press, Taylor and Francis, London, 2009), pp. 576.
- <sup>25</sup>H. Zaidi and B. M. W. Tsui, "Review of computational anthropomorphic anatomical and physiological models," *Proc. IEEE* **97**, 1938–1953 (2009).
- <sup>26</sup>R. Tanaka, S. Mitomo, and N. Tamura, "Effects of temperature, relative humidity, and dose rate on the sensitivity of cellulose triacetate dosimeters to electrons and [gamma]-rays," *Int. J. Appl. Radiat. Isotopes* **35**, 875–881 (1984).
- <sup>27</sup>H. Levine, W. L. McLaughlin, and A. Miller, "Temperature and humidity effects on the gamma-ray response and stability of plastic and dyed plastic dosimeters," *Radiat. Phys. Chem.* (1977) **14**, 551–574 (1979).
- <sup>28</sup>B. Whittaker and M. Watts, "The influence of dose rate, ambient temperature and time on the radiation response of Harwell PMMA dosimeters," *Radiat. Phys. Chem.* **60**, 101–110 (2001).
- <sup>29</sup>H. Zaidi, "Relevance of accurate Monte Carlo Modeling in nuclear medical imaging," *Med. Phys.* **26**, 574–608 (1999).
- <sup>30</sup>K. S. Kolbert *et al.*, "Murine S factors for liver, spleen, and kidney," *J. Nucl. Med.* **44**, 784–791 (2003).
- <sup>31</sup>T. Funk, M. Sun, and B. H. Hasegawa, "Radiation dose estimate in small animal SPECT and PET," *Med. Phys.* **31**, 2680–2686 (2004).
- <sup>32</sup>W. H. Ellet and R. M. Humes, "MIRD Pamphlet No. 8: Absorbed fractions for small volumes containing photon-emitting radioactivity," *J. Nucl. Med.* **12**, 25–32 (1971).
- <sup>33</sup>A. Bitar *et al.*, "A voxel-based mouse for internal dose calculations using Monte Carlo simulations (MCNP)," *Phys. Med. Biol.* **52**, 1013–1025 (2007).
- <sup>34</sup>P. H. R. Peixoto, J. W. Vieira, H. Yoriyaz, and F. R. A. Lima, "Photon and electron absorbed fractions calculated from a new tomographic rat model," *Phys. Med. Biol.* **53**, 5343–5355 (2008).
- <sup>35</sup>T. Xie, D. Han, Y. Liu, J. Sun, and Q. Liu, "Skeletal dosimetry in a voxel-based rat phantom for internal exposures to photons and electrons," *Med. Phys.* **37**, 2167–2178 (2010).
- <sup>36</sup>T. Xie, G. Zhang, Y. Li, and Q. Liu, "Comparison of absorbed fractions of electrons and photons using three kinds of computational phantoms of rat," *Appl. Phys. Lett.* **97**, 33702–33704 (2010).
- <sup>37</sup>M. G. Stabin, T. E. Peterson, G. E. Holburn, and M. A. Emmons, "Voxel-based mouse and rat models for internal dose calculations," *J. Nucl. Med.* **47**, 655–659 (2006).
- <sup>38</sup>M. A. Keenan, M. G. Stabin, W. P. Segars, and M. J. Fernald, "RADAR realistic animal model series for dose assessment," *J. Nucl. Med.* **51**, 471–476 (2010).
- <sup>39</sup>K. A. Cockell, P. W. Fischer, and B. Belonje, "Elemental composition of anatomically distinct regions of rat liver," *Biol. Trace Elem. Res.* **70**, 251–263 (1999).

- <sup>40</sup>W. Caster, J. Poncelet, A. Simon, and W. Armstrong, "Tissue weights of the rat. I. Normal values determined by dissection and chemical methods," *Proc. Soc. Exp. Biol. Med.* **91**, 122–126 (1956).
- <sup>41</sup>L. Garcia-Moreno *et al.*, "Behaviour of nucleolar organizer regions in the different Wistar rat liver lobes," *Lab. Anim.* **28**, 50–54 (1994).
- <sup>42</sup>X. Bai *et al.*, "A high-resolution anatomical rat atlas," *J. Anat.* **209**, 707–708 (2006).
- <sup>43</sup>L. Wu, G. Zhang, Q. Luo, and Q. Liu, "An image-based rat model for Monte Carlo organ dose calculations," *Med. Phys.* **35**, 3759–3764 (2008).
- <sup>44</sup>P. Popesko, V. Rajtová, and J. Horak, *A Colour Atlas of the Anatomy of Small Laboratory Animals* (Wolfe Publishing, London, 1992).
- <sup>45</sup>M. W. Konijnenberg, M. Bijster, E. P. Krenning, and M. De Jong, "A stylized computational model of the rat for organ dosimetry in support of pre-clinical evaluations of peptide receptor radionuclide therapy with (90)Y, (111)In, or (177)Lu," *J. Nucl. Med.* **45**, 1260–1269 (2004).
- <sup>46</sup>K. Gurusamy and B. R. Davidson, "Trace element concentration in metastatic liver disease: A systematic review," *J. Trace Elem. Med. Biol.* **21**, 169–177 (2007).
- <sup>47</sup>ICRU, *International Commission on Radiological Units and Measurements* (ICRU, 1989), Report No. 44.
- <sup>48</sup>ICRP, "Basic anatomical and physiological data for use in radiological protection: reference values: ICRP Publication 89," *Ann. ICRP* **32**, 1–277 (2002).
- <sup>49</sup>ICRU, *International Commission on Radiological Units and Measurements* (ICRU, 1992), Report No. 46.
- <sup>50</sup>W. E. Bolch, K. F. Eckerman, G. Sgouros, and S. R. Thomas, "MIRD Pamphlet No. 21: A generalized schema for radiopharmaceutical dosimetry—standardization of nomenclature," *J. Nucl. Med.* **50**, 477–484 (2009).
- <sup>51</sup>W. S. Snyder, M. R. Ford, G. G. Warner, and S. B. Watson, "S," *Absorbed Dose Per Unit Cumulated Activity for Selected Radionuclides and Organs. MIRD Pamphlet No. 11* (Society of Nuclear Medicine, New York, 1975).
- <sup>52</sup>D. B. Pelowitz, Los Alamos National Laboratory, NM; Report No. LA-CP-05-0369, 2005.
- <sup>53</sup>W. E. Bolch *et al.*, "MIRD pamphlet No. 17: the dosimetry of nonuniform activity distributions—Radionuclide S-values at the voxel level. Medical Internal Radiation Dose Committee," *J. Nucl. Med.* **40**, 11S–36S (1999).
- <sup>54</sup>B. Walters, I. Kawrakow, and D. Rogers, *Ionizing Radiation Standards* National Research Council of Canada; Report No. PIRS-794revB, 2005.
- <sup>55</sup>J. A. Siegel and M. G. Stabin, "Mass scaling of S-values for blood-based estimation of red marrow absorbed dose: The quest for an appropriate method," *J. Nucl. Med.* **48**, 253–256 (2007).
- <sup>56</sup>M. G. Stabin, "Uncertainties in internal dose calculations for radiopharmaceuticals," *J. Nucl. Med.* **49**, 853–860 (2008).
- <sup>57</sup>F. Paquet, S. Frelon, G. Cote, and C. Madic, "The contribution of chemical speciation to internal dosimetry," *Radiat. Prot. Dosimetry* **105**, 179–184 (2003).
- <sup>58</sup>J. E. Turner, "Interaction of ionizing radiation with matter," *Health Phys.* **88**, 520–544 (2005).
- <sup>59</sup>W. Bult, M. A. Vente, B. A. Zonnenberg, A. D. Van Het Schip, and J. F. Nijsen, "Microsphere radioembolization of liver malignancies: current developments," *Q. J. Nucl. Med. Mol. Imaging* **53**, 325–335 (2009).